ChemComm

COMMUNICATION

View Article Online
View Journal

Cite this: DOI: 10.1039/d6cc00567e

Received 27th January 2026,
Accepted 2nd March 2026

DOI: 10.1039/d6cc00567e

rsc.li/chemcomm

Structural domain plasticity drives Zn(II) distribution and buffering in metallothionein-3

Manuel David Peris-Díaz, [ab] Eduard H. T. M. Ebberink,[a] Jan Fiala, [a] Albert J. R. Heck [a] and Artur Krężel *[b]

Complementary mass spectrometry-based approaches and molecular dynamics simulations were integrated to map Zn(II) distribution in partially metalated Zn_{4-6}-metallothionein-3 species relevant to zinc metabolism. Sequential Zn(II) dissociation engages both the α- and β-domains through a structurally plastic, interdomain mechanism that underpins regulatory zinc buffering at physiological pZn.

In mammals, the metallothionein (MT) protein family comprises four major isoforms (MT1–MT4) and multiple MT1 subisoforms, which differ in metal-binding preferences, tissue distribution, and cellular localization.[1] While MT1 and MT2 are ubiquitously expressed across all tissues, MT3 is primarily found in the brain. However, many reports suggest a critical role for MT3 in other tissues as well.[2–4] In the central nervous system (CNS), MT3 regulates synaptic zinc signaling and protects against neurodegeneration, swapping Zn(II) ions for excess Cu(II)/Cu(I).[5,6] Recent studies have expanded MT3's functional relevance beyond the CNS, for instance, Mo *et al.*, showed that MT3 is the dominant MT isoform expressed in osteoclasts, and plays a vital role in osteoclastogenesis and bone metabolism by regulating intracellular Zn(II) concentrations.[7] Salvagio *et al.* showed that MT3 was a source of zinc spikes in neurons, acting as a regulatory signal during neuronal development,[8] and Tran *et al.* demonstrated a critical role for MT3 in Zn(II) homeostasis underlying protective immune functions.[9] Yet the molecular basis of how MTs donate/accept Zn(II) remains poorly understood.[1] This is largely because MTs are small (~6–7 kDa), cysteine-rich proteins lacking stable secondary structure and aromatic residues, whereas Zn(II) is spectroscopically silent. Consequently, only one X-ray structure of mammalian MT (mixed complex of rat Cd_5Zn_2MT2) has been solved to date.[10] In that structure, the protein folds into a dumbbell-shaped structure, with two metal/sulfur clusters located in two α and β domains.[11] In the presence of soft or medium soft divalent metal ions (M(II)), the 20 cysteine residues (21 in MT1b) can assemble metal/sulfur clusters within the β- and α-domains resulting in M_3Cys_9 and M_4Cys_{11} cores, respectively, when fully saturated.[12–14] However, at physiological labile Zn(II) concentrations ($[Zn(II)]_{labile}$) MT is present as partially metalated species (Zn_{4-6}MT) due to differences in zinc sites' affinity.[1,15] The unsaturated nature of those species allows them to function as buffer molecules, as shown for MT2, keeping labile Zn(II) at the right pZn level (pZn = -log$[Zn(II)]_{labile}$), and act as Zn(II) donors and acceptors when needed.[15–19] How Zn(II) is distributed within MT3 across these Zn_{4-6}MT3 species, and how this distribution affects properties, remains unknown and is a focus of this study.

MT3 also differs functionally from other MTs, as unlike MT1-2, MT3 is generally not strongly metal-inducible.[1] Nevertheless, recent studies suggest MT3 is highly upregulated during osteoclast differentiation and is crucial for Zn(II) buffering during osteoclastogenesis.[7,20] Structurally, MT3 is the only isoform with two β-domain prolines in the T_5CPCP_9 motif, and an acidic hexapeptide loop in the α-domain. Despite these differences, isothermal titration calorimetry (ITC) measurements of Zn(II) binding to MT3 revealed three thermodynamically distinct binding populations, similar to those observed for MT2.[21]

To investigate the structural and dynamical response of MT3 to Zn(II) binding and to define the microscopic organization of these partially Zn(II)-loaded MT3 species, we combined chemical labeling mass spectrometry (MS), top-down (TD)-MS, ion mobility-MS, and molecular dynamics (MD) simulations. The number of cysteine residues coordinating Zn(II) across the Zn_{1-7}MT3 series was determined using a differential thiol-labeling strategy (Fig. S1). In the first step, iodoacetamide (IAM; +57.0215 Da per modified cysteine residue) was used to induce stepwise Zn(II) dissociation from Zn_7MT3, and the resulting $Zn_{7-x}IAM_y$MT3 species were measured by native MS.[22] IAM alkylates cysteine residues *via* an S_N2 mechanism, forming *S*-carbamidomethyl cysteine adducts and thereby

[a] *Biomolecular Mass Spectrometry and Proteomics, Bijvoet Center for Biomolecular Research and Utrecht Institute for Pharmaceutical Sciences, Utrecht University, Utrecht 3584 CH, The Netherlands*
[b] *Department of Chemical Biology, Faculty of Biotechnology, University of Wroclaw, F. Joliot-Curie 14a, 50-383, Wrocław, Poland. E-mail: artur.krezel@uwr.edu.pl*

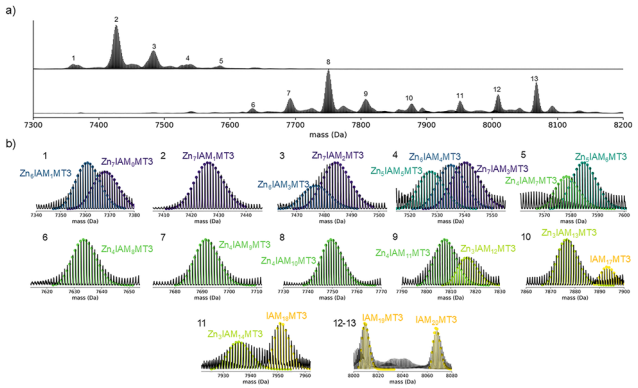

Fig. 1 Zero-charge mass distribution of Zn_7MT3 and reaction products after incubation with 25 mM (top) or 150 mM (bottom) iodoacetamide (IAM) (a). Experimental mass distributions were fit to the simulated theoretical isotopic distribution for candidate composition, and the best-fitting model is shown (b). Theoretical isotopic distributions were plotted as stem plots. Numbers above peaks in (a) label the assigned species and are used as identifiers throughout the manuscript.

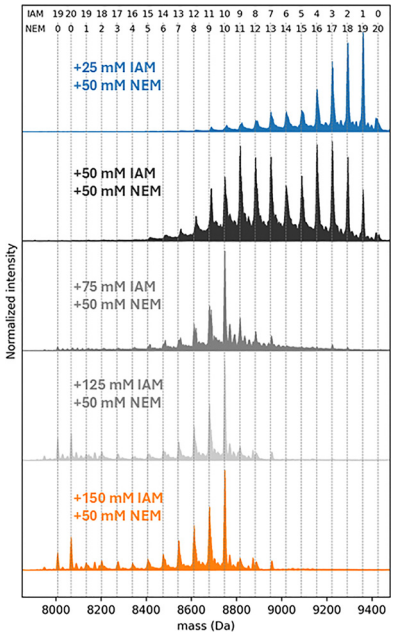

Fig. 2 Zero-charge mass distribution of products formed after the dual-labeling strategy. Zn_7MT3 proteins (30 μM) were incubated with 25, 50, 75, 125, or 150 mM iodoacetamide (IAM) in the dark at 25 °C for 15 min. Samples were desalted, and 50 mM *N*-ethylmaleimide (NEM) was added (30 min, 25 °C). Numbers above the plot indicate the number of incorporated IAM and NEM moieties.

increasing the protein mass by +57.0215 Da per modified cysteine residue. As this reaction requires the availability of nucleophilic thiolates, the weakest Zn(II)-thiolate sites are expected to react first.[23] To annotate the Zn(II):IAM stoichiometries, theoretical isotopic distributions for candidate compositions were simulated and compared with the experimental spectra, and the best-fitting model was selected (Fig. 1).

The deconvolved mass distribution of Zn_7MT3 incubated with 25–50 mM IAM showed that up to two IAM molecules react without Zn(II) dissociation, suggesting that up to two cysteine residues are free or only weakly coordinated to Zn(II) (Fig. 1, peak 2–3). We therefore verified the number of Zn(II)-coordinating cysteine residues by chelating the remaining bound Zn(II) and labeling the newly accessible thiols with *N*-ethylmaleimide (NEM), which reacts with cysteine residues *via* Michael addition to form thioether adducts (+125.0477 Da per modified Cys). This provides a readout of the cysteine residues previously bound to Zn(II). These experiments confirm that 19 cysteine residues selectively coordinate all seven Zn(II) ions and that one cysteine is only weakly involved in Zn(II) coordination (Fig. 2).

Next, we aimed to identify the IAM-labeled cysteine residues in Zn_7MT3 using native top-down MS. However, overlapping ions between $Zn_6IAM_3MT3^{5+}$ and $Zn_7IAM_2MT3^{5+}$ prevented quadrupole isolation and fragmentation of the latter species (Fig. 1b, peak 3). Instead, $Zn_7IAM_1MT3^{5+}$ ions were quadrupole-selected and subjected to collision-induced dissociation (CID). The resulting spectra showed limited backbone fragmentation, preventing localization of the IAM modification, most likely because Zn(II) shields the backbone from cleavage (Fig. S2). Only terminal *b*- and high-mass *y*-ions were observed, neither of which provided site-localization information.

We therefore performed TD CID-MS on the doubly labeled $NEM_{19}IAM_2MT3^{5+}$ ions, with IAM reporting on free cysteine residues and NEM identifying cysteines that had previously coordinated Zn(II). Specifically, quadrupole-isolated $NEM_{19}IAM_2MT3^{5+}$ ions were subjected to collisional activation (CA), generating *b*-fragment ions b6–b11 that show Cys6 and Cys8 are IAM-labeled. The *y*-fragment ions y60–y66 further corroborated this assignment (Fig. S3).

The third and fourth IAM modifications triggered Zn(II) dissociation, yielding Zn_6IAM_3MT3 and Zn_6IAM_4MT3 species (Fig. 1, peak no. 3–4). After dual labeling, we estimated that 16–17 cysteine residues predominantly coordinate the six Zn(II) ions (Fig. 2). When $NEM_{16}IAM_4MT3^{5+}$ ions were quadrupole-isolated and analyzed by TD CID-MS, the resulting spectra contained *b*-fragment ions b6–b10, consistent with IAM modification of Cys6 and Cys8, together with *y*-fragment ions y55–y66 that confirm this assignment. Although we could not unambiguously locate the remaining two Cys-IAM modifications, the overall fragmentation patterns hint that the seventh Zn(II) ion is bound in the β-domain (Fig. S4). Because the structural resolution was limited, we complemented these MS experiments with steered molecular dynamics (SMD) simulations. SMD was used to rank Zn(II) binding sites according to the work required for metal dissociation, thereby inferring plausible partially Zn(II)-loaded MT3 forms.

Consistent with the TD CID-MS results, SMD identified the weakest Zn(II) site as a β-domain site in which Zn(II) is coordinated by Cys6, Cys8, Cys22, and Cys25 (Fig. 3a). The resulting Zn_6MT3 structure features a Zn_2Cys_6 cluster in the β-domain, with three cysteines completely free and solvent molecules entering the coordination sphere (Fig. S5).

Subsequent IAM modification led to dissociation of a second Zn(II) ion, forming $Zn_5IAM_{5-6}MT3$ species (Fig. 1b peak 4–5). Dual-labeling experiments determined that 14–15 cysteine

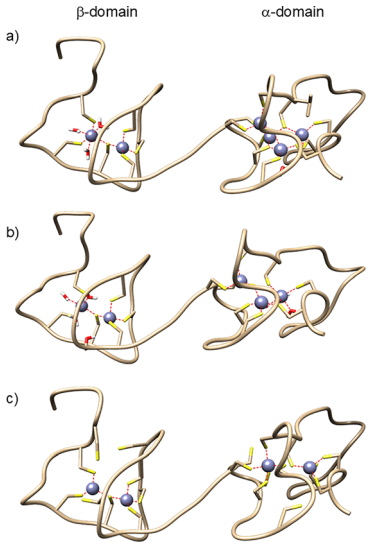

Fig. 3 Representative frames of Zn_6MT3 (a), Zn_5MT3 (b), and Zn_4MT3 (c) species from steered molecular dynamics simulations (SMD) trajectories. The total work required to dissociate each Zn(II) ion from its binding site in each Zn(II)-loaded MT3 protein is shown in Table S1. Sulfur atoms and Zn(II) ions are shown in yellow and gray, respectively, and the protein backbone in licorice representation. Zn–S interactions, defined by a distance of <2.5 Å, are shown as red dashed lines.

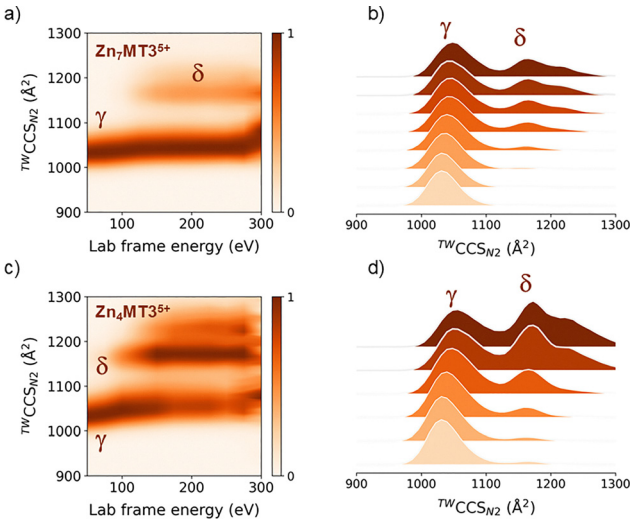

Fig. 4 Collision-induced unfolding (CIU) heat maps (a) and (c) and travelling wave (TW)-derived collision cross sections ($^{TW}CCS_{N2}$) profiles (b) and (d) for quadrupole-selected Zn_7MT3^{5+} and Zn_4MT3^{5+} ions. Proteins (10 μM) were nanoESI-sprayed from 200 mM ammonium acetate (pH 6.8) in the presence of 1 mM neutralized TCEP (pH 7.4). Note that the alpha and beta numbering in the figure refers to folded and unfolded states, not to the protein domain.

residues coordinate the five Zn(II) ions (Fig. 2). TD CID–MS of $NEM_{14}IAM_6MT3^{5+}$ showed multiple C-terminal *y*-fragment ions that were IAM-labeled, indicating Zn(II) dissociation from the α-domain (Fig. S6). Moreover, *y*-fragment ions y52–y66 supported that Cys6 and Cys8 were also IAM-labeled. In line with this, SMD simulations identified Zn(II) dissociation from the α-domain, yielding a structure with a Zn_3Cys_9 cluster in the α-domain and a Zn_2Cys_6 cluster in the β-domain (Fig. 3b). Dissociation of the third Zn(II) ion generated $Zn_4IAM_{8-10}MT3^{5+}$ ions (Fig. 1, peak no. 6–9). Conventional top-down MS using CID did not provide any new additional fragmentation, either when comparing the singly labeled $Zn_4IAM_{8-10}MT3$ and Zn_5IAM_{5-6}-MT3 species or when comparing the doubly labeled species $NEM_{14}IAM_6MT3$ and $NEM_{10-12}IAM_{10-8}MT3$. Electron-based fragmentation methods have previously been shown to enable metal-binding site localization in several metalloproteins.[24] We therefore employed top-down electron transfer dissociation (ETD) and electron transfer/higher-energy collisional dissociation (EThcD), but only nondissociative electron transfer dissociation (ETnoD) was observed, leading to electron–capture charge reduction (Fig. S7). To improve fragmentation and site localization, we applied top-down ultraviolet photodissociation (UVPD) on quadrupole-isolated $NEM_{10}IAM_{10}MT3^{5+}$ ions, which yielded extensive protein backbone fragmentation and sequence coverage (Fig. S8).

The resulting fragmentation map shows that up to 3 cysteines are IAM-modified and 6 are NEM-modified in the β-domain, consistent with SMD simulations, which depict a Zn_4MT3 structure in which the β-domain contains a Zn_2Cys_6 cluster and 3 free cysteine residues. TD-UVPD and SMD results point toward a configuration in which Zn(II) is redistributed between the α- and β-domains (Fig. 3c).

To assess whether this redistribution is accompanied by global conformational changes, we examined partially Zn(II)-loaded MT3 species by native travelling-wave ion mobility MS (TWIM-MS). Zn_7MT3 shows a collision cross-section ($^{TW}CCS_{N2}$) distribution dominated by a single conformer centered at ~1071 Å^2 (Fig. S9). Zn(II) dissociation from Zn_7MT3 to form Zn_4MT3 does not induce a major shift to a more extended conformation, only a low-intensity conformer appears centred at ~1180 Å^2 (Fig. S9).

To probe conformational families and unfolding pathways, we applied collisional activation to quadrupole-selected ions and recorded TWIM-MS spectra (Fig. 4). CA of the ~1071 Å^2 γ conformer leads to a minor δ conformer at ~1180 Å^2 (Fig. 4a).

The same conformer is also observed for quadrupole-selected Zn_4MT3^{5+} ions and becomes the predominant conformation upon activating conditions. Together, these data indicate that the ~1180 Å^2 conformer is present in all Zn(II)-loaded MT3 forms and is therefore not uniquely determined by metal content. While TWIM-MS reports on gas-phase conformational families and does not directly reflect in solution-phase structures, the broadly similar unfolding behavior observed for Zn_7MT3 and Zn_4MT3 suggests comparable global stability features. In combination with TD-UVPD and SMD results, this supports a model in which four Zn(II) ions are coordinated across both domains, since a configuration with one completely metal-free domain would be expected to induce a more pronounced conformational shift. Therefore, both the α- and β-domains appear to be required features of metallothioneins for regulatory Zn(II) buffering.

In our previous study, Zn_7MT2 was observed to undergo complete unfolding to a highly extended conformation at ~100 eV.[23] By contrast, Zn_7MT3 exhibits only partial unfolding, with the compact ~1071 Å^2 γ conformer dominating the conformational landscape. This indicates that Zn_7TM3 adopts a more stable conformation than Zn_7MT2. This observation agrees with previous studies showing an enhanced resistance of MT3 to proteolysis, suggesting that MT3 is stabilized in a thermodynamically favorable conformation that may be relevant to its specific biological function.[25–28] Despite this increased structural stability, MT3 binds Zn(II) more weakly than MT2.[29–33] Experiments with EDTA demonstrate that Zn_7MT3 has a higher metal-transfer potential than Zn_7MT2, indicating that resistance to unfolding is not directly correlated with Zn(II)-binding affinity, but instead confers MT3 with unique functional properties, which might be connected to its intra- and extracellular functions.[24,33] For example, studies using Zn(II)-reconstituted domain peptides have shown that *S*-nitrosothiols dissociate Zn(II) from both the α- and β-domains of MT3, but not from MT2.[34] Consistently, cell-based studies demonstrate that MT3 provides significantly stronger protection against *S*-nitrosothiols, as it is the only metallothionein isoform containing consensus acid–base sequence motifs for *S*-nitrosylation in both domains. Functional studies further indicate that the N-terminal β-domain is necessary for growth-inhibition activity, whereas the C-terminal α-domain may be dispensable for GIF activity.[35,36]

Mutational studies identified two conserved prolines and a threonine within a distinctive TCPCP motif in the N-terminal β domain of MT3 as essential for GIF activity.[29,35,37] This TCPCP motif, which is absent in other metallothionein isoforms, contributes to the unique structural and metal-binding properties of MT3. Through its β-domain, MT3 protects against copper toxicity by scavenging free Cu(II) ions or removing Cu(II) bound to β-amyloid and α-synuclein.[38–40] The enhanced structural plasticity of the β-domain likely underpins these functions. Altogether, MT3 is a unique biologically active neuronal growth-inhibitory factor.

Overall, our study provides new insights into the architecture, stability, and dynamics of Zn(II)-MT3 and links these features to its metal buffering properties, underscoring its key role in regulating zinc and copper levels in the human body.

This research was supported by the National Science Centre of Poland (NCN) under the Opus grant no. 2021/43/B/NZ1/02961.

Conflicts of interest

There are no conflicts to declare.

Data availability

The data supporting this article have been included as part of the supplementary information (SI). Supplementary information: the mass spectrometry data have been deposited in the Figshare repository (https://doi.org/10.6084/m9.figshare.31436293). See DOI: https://doi.org/10.1039/d6cc00567e.

References

1 A. Krężel and W. Maret, *Chem. Rev.*, 2021, **121**, 14594–14648.
2 Y. Uchida, K. Takio, K. Titani, Y. Ihara and M. Tomonaga, *Neuron*, 1991, **7**, 337–347.
3 M. Vašák and G. Meloni, *Int. J. Mol. Sci.*, 2017, **18**, 1117.
4 J. Y. Koh and S. J. Lee, *Mol. Brain*, 2020, **13**, 116.
5 G. Meloni, V. Sonois, T. Delaine, L. Guilloreau, A. Gillet, J. Teissié, P. Faller and M. Vašák, *Nat. Chem. Biol.*, 2008, **4**, 366–372.
6 N. E. Wezynfeld, E. Stefaniak, K. Stachucy, A. Drozd, D. Płonka, S. C. Drew, A. Krężel and W. Bal, *Angew. Chem., Int. Ed.*, 2016, **55**, 8235–8238.
7 S. Mo, M. K. Kim, J. S. Jang, S. H. Lee, S. J. Hong, S. Jung and H. H. Kim, *Exp. Mol. Med.*, 2024, **56**, 1791–1806.
8 L. Salvagio, C. Zhang, B. E. Rue, N. Doris, C. Koehring, I. Tyler, R. S. Vargas, W. C. Oh and Y. Qin, *J. Neurosci.*, 2025, **45**, e0627252025.
9 N. B. Tran and S. J. Lee, *Cell Death Discovery*, 2025, **11**, 45.
10 A. H. Robbins, D. E. McRee, M. Williamson, S. A. Collett, N. H. Xuong, W. F. Furey, B. C. Wang and C. D. Stout, *J. Mol. Biol.*, 1991, **221**, 1269–1293.
11 W. Braun, M. Vašák, A. H. Robbins, C. D. Stout, G. Wagner, J. H. Kägi and K. Wüthrich, *Proc. Natl. Acad. Sci. U. S. A.*, 1992, **89**, 10124–10128.
12 D. W. Hasler, P. Faller and M. Vašák, *Biochemistry*, 1998, **37**, 14966–14973.
13 P. Faller, D. W. Hasler, O. Zerbe, S. Klauser, D. R. Winge and M. Vašák, *Biochemistry*, 1999, **38**, 10158–10167.
14 H. Wang, Q. Zhang, B. Cai, H. Li, K. H. Sze, Z. X. Huang, H. M. Wu and H. Sun, *FEBS Lett.*, 2006, **580**, 795–800.
15 A. Krężel and W. Maret, *J. Am. Chem. Soc.*, 2007, **129**, 10911–10921.
16 A. Krężel and W. Maret, *J. Biol. Inorg. Chem.*, 2006, **11**, 1049–1062.
17 K. Mosna, K. Jurczak and A. Krężel, *Metallomics*, 2023, **15**, mfad061.
18 A. Krężel and W. Maret, *J. Biol. Inorg. Chem.*, 2008, **13**, 401–409.
19 M. D. Peris-Díaz, R. Guran, C. Domene, V. de Los Rios, O. Zitka, V. Adam and A. Krężel, *J. Am. Chem. Soc.*, 2021, **143**, 16486–16501.
20 S. Arisumi, T. Fujiwara, K. Yasumoto, T. Tsutsui, H. Saiwai, K. Kobayakawa, S. Okada, H. Zhao and Y. Nakashima, *Cell Death Discovery*, 2023, **9**, 436.
21 M. C. Carpenter, A. Shami Shah, S. DeSilva, A. Gleaton, A. Su, B. Goundie, M. L. Croteau, M. J. Stevenson, D. E. Wilcox and R. N. Austin, *Metallomics*, 2016, **8**, 605–617.
22 S. Tamara, M. A. den Boer and A. J. R. Heck, *Chem. Rev.*, 2022, **122**, 7269–7326.
23 M. D. Peris-Díaz, A. Barkhanskiy, E. Liggett, P. Barran and A. Krężel, *Chem. Commun.*, 2023, **59**, 4471–4474.
24 P. Wongkongkathep, J. Y. Han, T. S. Choi, S. Yin, H. I. Kim and J. A. Loo, *J. Am. Soc. Mass Spetrom.*, 2018, **29**, 1870–1880.
25 R. Lakha, C. Hachicho, M. R. Mehlenbacher, D. E. Wilcox, R. N. Austin and C. L. Vizcarra, *J. Inorg. Biochem.*, 2023, **242**, 112157.
26 M. Knipp, G. Meloni, B. Roschitzki and M. Vašák, *Biochemistry*, 2005, **44**, 3159–3165.
27 J. S. Calvo, R. L. E. Villones, N. J. York, E. Stefaniak, G. E. Hamilton, A. L. Stelling, W. Bal, B. S. Pierce and G. Meloni, *J. Am. Chem. Soc.*, 2022, **144**, 709–722.
28 A. T. Yuan and M. Stillman, *FEBS J.*, 2025, **292**, 619–634.
29 D. W. Hasler, L. T. Jensen, O. Zerbe, D. R. Winge and M. Vašák, *Biochemistry*, 2000, **39**, 14567–14575.
30 M. C. Carpenter, A. Shami Shah, S. DeSilva, A. Gleaton, A. Su, B. Goundie, M. L. Croteau, M. J. Stevenson, D. E. Wilcox and R. N. Austin, *Metallomics*, 2016, **8**, 605–617.
31 C. F. Quinn and D. E. Wilcox, *Metallomics*, 2024, **16**, mfae041.
32 J. S. Calvo, V. M. Lopez and G. Meloni, *Metallomics*, 2018, **10**, 1777–1791.
33 P. Palumaa, E. Eriste, O. Njunkova, L. Pokras, H. Jörnvall and R. Sillard, *Biochemistry*, 2002, **41**, 6158–6163.
34 Y. Chen, Y. Irie, W. M. Keung and W. Maret, *Biochemistry*, 2002, **41**, 8360–8367.
35 A. K. Sewell, L. J. Jensen, J. C. Erickson, R. D. Palmiter and D. R. Winge, *Biochemistry*, 1995, **34**, 4740–4747.

36 S. Somji, S. H. Garrett, M. A. Sens and D. A. Sens, *Toxicol. Sci*, 2006, **90**, 369–376.
37 B. Cai, Q. Zheng, X. C. Teng, D. Chen, Y. Wang, K. Q. Wang, G. M. Zhou, Y. Xie, M. J. Zhang, H. Z. Sun and Z. X. Huang, *J. Biol. Inorg. Chem.*, 2006, **11**, 476–482.
38 G. Meloni and M. Vašák, *Free Radical Biol. Med.*, 2011, **50**, 1471–1479.
39 G. Meloni, P. Faller and M. Vašák, *J. Biol. Chem.*, 2007, **282**, 16068–16078.
40 A. Melenbacher and M. J. Stillman, *FEBS J.*, 2023, **290**, 4316–4341.